optica

Amplifiers of free-space terahertz radiation

Tsung-Yu Kao,[1,2,*] John L. Reno,[3] and Qing Hu[2]

[1]LongWave Photonics LLC, Mountain View, California 94043, USA
[2]Department of Electrical Engineering and Computer Science, Massachusetts Institute of Technology, Cambridge, Massachusetts 02139, USA
[3]Sandia National Laboratories, Center of Integrated Nanotechnologies, MS 1303, Albuquerque, New Mexico 87185, USA
*Corresponding author: wilt_kao@longwavephotonics.com

Received 27 February 2017; revised 29 April 2017; accepted 1 May 2017 (Doc. ID 287556); published 23 June 2017

Amplifiers of free-space radiation are quite useful, especially in spectral ranges where the radiation is weak and sensitive detectors are hard to come by. A preamplification of the said weak radiation signal will significantly boost the S/N ratio in remote sensing and imaging applications. This is especially true in the terahertz (THz) range where the radiation signal is often weak and sensitive detectors require the cooling of liquid helium. Although quantum cascade structures are promising for providing amplification in the terahertz band from 2 to 5 THz, a THz amplifier has been demonstrated in an integrated form, in which the source is in close proximity to the amplifier, which will not be suitable for the aforementioned applications. Here we demonstrate what we believe is a novel approach to achieve significant amplification of free-space THz radiation using an array of short-cavity, surface-emitting THz quantum cascade lasers operating marginally below the lasing threshold as a Fabry–Perot amplifier. This free-space "slow light" amplifier provides 7.5 dB(×5.6) overall gain at ∼3.1 THz. The proposed devices are suitable for low-noise pre-amplifiers in heterodyne detection systems and for THz imaging systems. With the sub-wavelength pixel size of the array, the reflective amplifier can also be categorized as active metasurface, with the ability to amplify or absorb specific frequency components of the input THz signal.

OCIS codes: (140.5965) Semiconductor lasers, quantum cascade; (140.5960) Semiconductor lasers; (140.3280) Laser amplifiers; (140.4480) Optical amplifiers; (250.5980) Semiconductor optical amplifiers.

https://doi.org/10.1364/OPTICA.4.000713

Terahertz (THz) heterodyne receivers are indispensable instruments with high sensitivity and spectral resolution to study star and galaxy formation through the observations of interstellar medium (ISM) [1] or to monitor gas radicals related to the ozone destruction process [2]. However, a low-noise amplifier (LNA), a key component widely used in a heterodyne detection system in the lower frequency range (for example, transistor amplifiers at millimeter-wave frequencies), is still lacking in THz frequency. Although THz quantum cascade structures are promising devices for providing amplification in the THz frequency, a THz amplifier has been mostly demonstrated in an integrated platform [3,4] in which the source and the amplifier are fabricated monolithically on the same wafer and also near-field coupled. The single-pass amplification is also limited by the strong facet reflection of the THz waveguide. One clever method to circumvent this limitation is to use the transient state of the lasing process through fast gain switching [5,6]. While high amplification is obtained, this technique requires careful synchronization between the timing of the switching signal and input pulse, and is only limited for short pulse amplification with the duration shorter than the gain recovery time (<100 ps).

Optical amplifiers can be categorized into two types [7]: traveling-wave amplifier (TWA), where cavity feedback is minuscule [8], and Fabry–Perot amplifier (FPA), where the cavity resonance effect is prevailing and the signal is effectively trapped inside the cavity, experiencing multiple pass amplification before escaping (see Fig. 1). Similar enhancement in gain can be observed in any type of resonance structure near its resonance frequency [9]. With an inherent strong facet reflection of metal–metal waveguides, THz QCL falls naturally into the latter category. Here we report what we believe is a novel approach to operate an array of surface-emitting THz quantum cascade lasers (QCL) slightly below its lasing threshold as a "slow light" amplifier for free-space THz radiation amplification at ∼3.1 THz with a 7.5 dB overall signal gain.

With short and narrow second-order DFB lasers similar to devices in Refs. [10,11], it is possible to construct a two-dimensional (2D) amplifier "grid" that has subwavelength element-to-element distance. A similar idea has been demonstrated using active diode amplifiers placed on rectangular metal meshes to form a grid amplifier in a microwave frequency [12]. Each active element only amplifies part of the total input signal. The amplified signal is then coherently combined in the far field. This "divide-and-conquer" approach overcomes the drawback of a low power saturation level for short cavity Fabry–Perot amplifiers.

Figure 2(c) shows the magnetic fields of the surface-emitting mode of a metal–metal waveguide second-order DFB THz laser from 3D full-wave finite element (FEM) simulations. In these simulations, the surface-emitting lasing mode is at 3.478 THz with a ∼31cm^{-1} mirror loss α_m. This structure is then placed inside a hemisphere (scattering boundary condition) with uniform plane-wave excitation (electric field magnitude = 1 V/m) directly from the top of the hemisphere [Fig. 2(a)]. The frequency of the excitation electric field and the material gain of the second-order DFB laser are both scanned near the resonance condition of

the amplifier. Figure 2(b) shows the reflected electric field after amplification (with the excitation field subtracted) near the resonance frequency. The direction of excitation field is also scanned.

The resonance-enhanced amplification can also be verified in the FEM simulation. The overall amplifier gain is defined as the total power flow outward through the hemisphere over the total input power. The input power can be calculated using the area of the circular bottom of the hemisphere times the input power flow per unit area. Figure 2(e) shows the gain versus frequency plot with different material gains under vertical plane-wave excitation. Excited near the resonance frequency, when the material gain increases from 28 cm^{-1} to 31 cm^{-1} (as the bias is increased close to the lasing threshold of the DFB laser), the overall gain increases from 13 to 30 dB and the bandwidth of the amplifier also decreases from ~4 GHz to sub-GHz. It is worth pointing out that when the material gain is higher than the lasing threshold of the structure, the computed overall signal gain will actually become lower without taking into account the gain-saturation effect (see the gain curve corresponding to the 32 cm^{-1} material gain). This occurs because, for an FPA, the gain actually decreases when the close-loop gain exceeds unity (above the lasing threshold). However, this phenomenon can only be observed in simulations because the material gain can never exceed the lasing threshold in a real laser due to the gain-clamping effect.

The gain obtained in this simulation is based on the assumption of 100% collection efficiency. Using the same simulation setup, material losses can be introduced to the DFB laser structure. When no loss is present in the laser cavity, the total power outflow should equal the total input power. When loss is present, part of the input power coupled into the DFB cavity will be absorbed. Although only ~5% of the surface area is occupied by the DFB laser (15 μm × 270 μm on a circular disc with a 320 μm diameter), that is, a filling factor of 0.05, more than 10% of input power is absorbed by the DFB cavity. In other words, the input coupling loss is ~90% for this single-element Fabry–Perot amplifier. The simulation also shows that the "effective cross-section area of the antenna" of the second-order DFB laser is roughly twice its physical size. Similar enhanced absorptions have been reported in Refs. [13,14].

From the simulation, we could see that the field distribution of a 9-period DFB laser is very concentrated in the center 3–5 periods, which suggests that even DFB lasers with a shorter cavity can be used without increasing the mirror loss dramatically. Indeed, the mirror loss for the surface-emitting mode of a 3-period DFB laser is only 36 cm^{-1} (compared to 31 cm^{-1} for the 9-period DFB). This 3-period short-cavity, second-order DFB laser can also be treated as a patch-antenna (length ~$\lambda/2$) with coupled-side antennas (length ~λ, where λ is the wavelength inside waveguide) attached to both ends to modify the far-field beam pattern. With a 36 cm^{-1} mirror loss and an 18 cm^{-1} estimated waveguide loss [15], a total ~54 cm^{-1} loss is obtained. Considering the peak gain is estimated to be 60–80 cm^{-1} for THz QCL gain materials at this frequency range [16], this mirror loss should increase the lasing threshold close to its maximum and fully use the gain of the material. Although one can potentially increase the mirror losses to beyond the lasing threshold, for Fabry–Perot amplifiers, to operate the amplifier at the optimal subthreshold gain value, it is crucial to choose a proper mirror loss value so that the lasing condition can still be met. At THz, since the radiation is invisible, to be able to reach the lasing threshold also makes optical alignment easier. The lasing spectra can also pinpoint the frequency range for maximum gain, as will be discussed later.

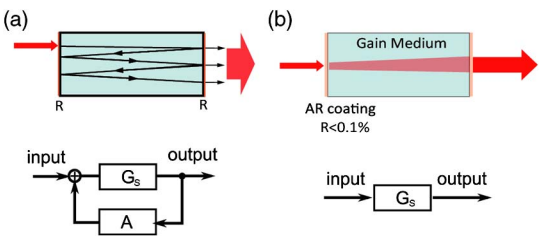

Fig. 1. Schematic for (a) Fabry–Perot amplifiers and (b) travelling-wave amplifier. For a TWA, anti-reflection coating on the facet between the dielectric gain medium and the free space is usually used to reduce the power reflectivity to <0.1%.

In the previous FEM simulation, amplifiers occupy only 5% of the reflected surface. To increase the area-filling factor, the dimensions of the DFB laser are carefully selected. Figure 3(c) shows the scanning electron microscopy (SEM) picture of a single-element 3-period, second-order DFB laser. The width of the laser is 15 μm with roughly 80 μm in total length. The laser is biased using the side contact fins similar to the one used in Ref. [17], which connect to the outer rectangular biasing "rim." The ridge width of the rim is ~10 μm. Each element is then used as a building block for the 2D grid amplifier. In one of the final designs, the lateral distance between adjacent elements is chosen to be 85 μm and the vertical distance is ~180 μm. Instead of being arranged in a standard rectangular grid, every other column of the elements is shifted by ~90 μm. Note that although this would not increase the device area-filling factor, the minimum vertical element distance is still effectively reduced by half. With the 85 × ~90 μm effective "pixel" size, an array with sub-wavelength element distance is achievable ($\lambda_0 \approx 100$ μm at 3 THz, the designed lasing frequency of the amplifier structure). The reflective amplifier structure can also be treated as an active frequency selective metasurface [18–20], with the ability to amplify or absorb specific

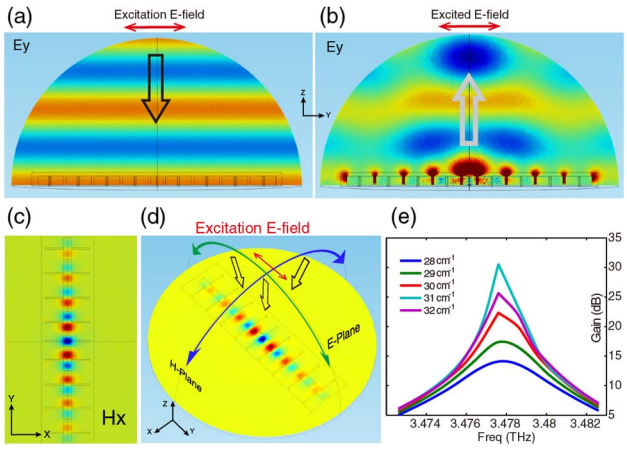

Fig. 2. Excited fields by plane-wave excitation along the E-plane of a 9-period, second-order DFB laser. (a) Excitation electric field. (b) Reflected electric field after amplification. (c) Magnetic field of the resonance mode for the 9-period, second-order DFB laser. (d) Definition of E-plane/H-plane direction. The excitation electric field polarization has no x-direction components. The arrows show the incident directions of plane-wave excitations. (e) Gain versus frequency plots from FEM simulation under different material gain values.

frequency components of the input signal. As seen in Fig. 3(a), the modified rectangular grid is then truncated to fit inside a circle with a ∼1.7 mm diameter. Four separated bonding pads are then attached to the grid using a series of spoke-like metal connectors. The grid is also electronically separated into four quadrants by removing part of the biasing rims. The dimensions of the whole amplifier device are roughly 2 × 2 mm with ∼120 identical surface-emitting DFB lasers. The overall device filling factor is ∼8%. A total of 30–40 different amplifier designs can be fabricated on the same wafer, each forming a 2.5 × 2.5 mm subchip. The devices are fabricated by standard contact lithography and inductively coupled plasma reactive-ion etch (ICP-RIE) using a self-aligned Ti/Au metal mask. The current is provided to each element through a network of metal contacts that all connect to a large bonding pad near the edge of the amplifier. The input source is a single-element surface-emitting DFB laser with equal dimensions and fabricated from the same gain medium (OWI-180E, 3-well resonant-phonon depopulation design with one well injector and a 180 repeated module; wafer number: VB0205). This is to ensure the source frequency is within the amplifier bandwidth. One of the many tested amplifiers, device # 3THZ R15 P3, which consists of 3-period DFB lasers with a 15-μm ridge width, is chosen for the demonstration of the THz amplifier.

The amplifier is being tested under the reflective configuration [Fig. 4(a)]. The single frequency emission from a single-element 9-period DFB THz QCL acts as the excitation "seed." The seed radiation is sent to the amplifier mounted inside a pulse-tube cryo-refrigerator (CryoMech PT-810) and operated continuously at ∼14–16 K. Each quadrant of the amplifier consumes roughly <300 mA current when biased marginally below the lasing threshold. The source laser is operated under pulsed mode (250–500 ns, 20–40 kHz, 1–2% duty-cycle) at 47–57 K inside a temperature-controlled, cryogen-free Stirling cooler (LongWave EasyQCL-100). The THz signal reflected from the amplifier is measured using a liquid helium-cooled Ge:Ga photodetector and a lock-in detected at the modulation frequency of the seed laser. The optical alignment is carefully adjusted and verified with the following procedures. First, the amplifier and the source laser are adjusted to be on the same optical plane. The seed THz radiation is then sent to the THz light amplifier using a single Si lens mounted on a XYZ stage for finer optical alignment. A flat mirror is used to the change direction of the input signal so that steep excitation angles can be achieved. Since the spot size of the focused THz beam is only a few wavelengths in diameter ($\lambda_0 \approx 100$ μm), and the amplifier is smaller than 2 mm, this is the most demanding alignment step. A NEC THz camera (model: IRV-T0831) is used to aid this task. The THz camera is used to image the THz light amplifier inside the cryostat at 10 K. Due to the difference in emissivity of materials, the outline of the THz amplifier is clearly shown. THz radiation from the seed laser can then be focused precisely on the THz amplifier through carefully adjusting the XYZ stage [see Fig. 4 (e)]. The camera is then replaced and the emission from the amplifier is collected using another Si lens and focused directly onto the photodetector. During measurements, finer alignment is performed by maximizing the amplified signal.

The pulsed spectra of the amplifier at 10 K at different biases above its lasing threshold are shown in the Fig. 5(a) inset. The amplifier has single-frequency emission at all bias ranges. A small blue shift in frequency can be observed when increasing the bias voltage. The CW spectra at 16 K are expected to be 2 GHz–3 GHz lower than the pulsed spectra due to frequency thermal tuning (∼200 MHz/K for THz DFB lasers). One can imagine the peak gain below the lasing threshold will be at slightly lower frequencies. Spectra from the seed laser at ∼50 K are also shown. Similar single-mode emission is obtained with only a small difference in frequency compared to the lasing spectra from the amplifier. The lasing frequency of the single-element device also shows a blue shift with bias

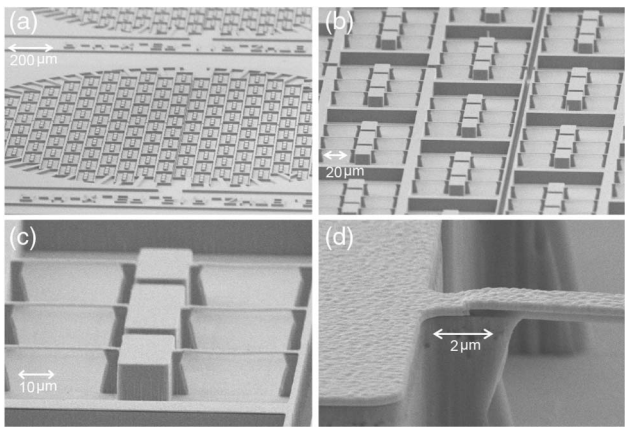

Fig. 3. SEM pictures for a typical THz radiation amplifier. (a) Overall view of the amplifier. (b) Close-up view of the same picture. (c) SEM picture of a single-element, 3-period device. (d) Zoom-in picture shows a clear air-bridge structure and its SiO_2 insulation layer.

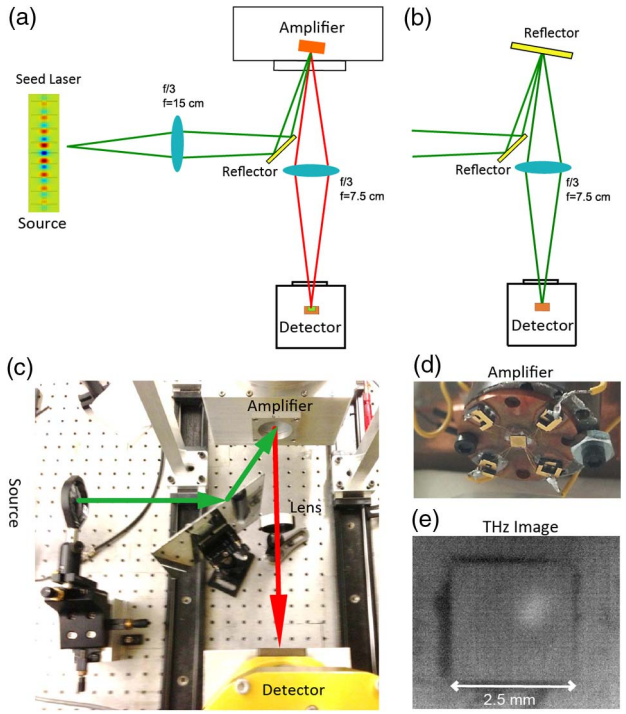

Fig. 4. (a) Schematic of optical setup for testing the THz radiation amplifier under reflection mode with another THz QC laser as the excitation source. (b) Schematic of optical setup for measuring reference power level at different source biases. (c) Picture of the optical setup in part (a). Seed laser beam path is depicted in green and the amplified signal beam path is in red. (d) Picture of a THz amplifier on a copper mount. (e) Real-time thermal image of the amplifier at 10 K taken with NEC THz imager. The THz radiation from the seed laser is focused onto the upper right quadrant of the amplifier (bright spot in the picture).

voltage. By changing both the bias and temperature of the seed laser, a frequency tunable source can be obtained.

Figure 5(a) shows the 2D plot of the detected THz power after reflecting from the amplifier at different amplifier and source bias voltages. The QCL material gain changes with the amplifier bias (gain scan). The frequency of the source laser will also change with the bias due to a Stark shift (frequency scan of the seed laser). A clear amplification peak is observed. To measure the system-level gain, i.e., the ratio of the power measured at the output port after and before the introduction the THz light amplifier, the optical setup in Fig. 4(b) is used. The amplifier is replaced with a high-reflective mirror placed roughly at the focal spot of the source laser relay system while keeping the position of other components in the system fixed. The reflective mirror is then fine-tuned to maximize the measured power, which formed the denominator in the gain calibration.

A detailed source bias scan is then performed to obtain the reference power level at every source bias. The measured reference power is shown in Fig. 5(b). Note that although the reference power can be measured in a more direct manner by simply placing the photodetector at the focal spot of the image relay system, the reference scheme used here also takes into account the power loss along the optical path due to strong atmosphere absorption at terahertz frequency range, which eliminates the need to purge the whole measurement setup.

Figure 5(c) shows the calibrated gain curves of the amplified signals as functions of different amplifier bias voltages (amplifier gain) under various seed laser bias points. Similar to the FEM simulation result, the amplification increases rapidly near the lasing threshold, and also strongly depends on the excitation frequency. A peak system-level gain of 5.6 × (7.5 dB) is obtained at source bias ∼12.1 V and amplifier bias ∼12.57 V (slightly below the lasing threshold ∼12.58 V). For this measurement, the seed laser is operated in pulsed mode at 47 K while the amplifier is DC biased at 16 K. From the photodetector and the lock-in amplifier output, the peak amplified signal is estimated to have ∼1 mW peak power (1% duty-cycle). The bandwidth (3 dB) of the THz light amplifier is estimated to be only ∼500 MHz from the spectra data of the source laser at different biases shown in Fig. 5(a). The in-coupling efficiency is estimated to be ∼16% (2 × of the overall filling-factor from the result of FEM simulations). In summary, we have successfully demonstrated what we believe is a novel approach to achieve a significant amplification of free-space THz radiation using an array of short-cavity, surface-emitting, second-order DFB THz quantum cascade lasers operating marginally below the lasing threshold as a Fabry–Perot amplifier. A 7.5 dB (×5.6) system-level gain is obtained with an estimated sub-GHz bandwidth. The signal gain can be further improved by increasing the filling factor (only ∼8% in this work) and the coupling efficiency. The limited bandwidth might be suitable or even desirable for applications such as preamplifiers for heterodyne detection systems targeting a specific spectral line or single frequency THz imaging.

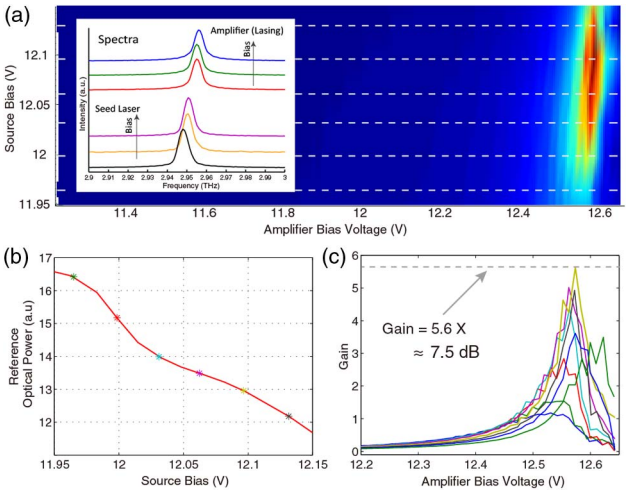

Fig. 5. (a) Two-dimensional surface plot of detected THz power after reflection from the amplifier at different amplifier and source bias. (inset) Pulsed spectra data from an amplifier device at 10 K. Spectra from seed laser are also shown. Both devices have single frequency emission at all bias. (b) Reference power level at different source biases. (c) Calibrated system-level gain curves of amplified signals under various amplifier/seed laser bias points.

Funding. National Aeronautics and Space Administration (NASA); National Science Foundation (NSF); Sandia National Laboratories; U.S. Department of Energy (DOE) (DE-AC04-94AL85000).

Acknowledgment. The authors would like to acknowledge Alan Lee from LongWave Photonics LLC, for the use of the EasyQCL-100 system.

REFERENCES

1. T. G. Phillips and J. Keene, Proc. IEEE **80**, 1662 (1992).
2. R. G. Prinn, J. Huang, R. F. Weiss, D. M. Cunnold, P. J. Fraser, P. G. Simmonds, A. McCulloch, C. Harth, P. Salameh, S. O. Doherty, R. H. J. Wang, L. Porter, and B. R. Miller, Science **292**, 1882 (2001).
3. C. Mauro, R. P. Green, A. Tredicucci, F. Beltram, H. E. Beere, and D. A. Ritchie, J. Appl. Phys. **102**, 063101 (2007).
4. H. Zhu, F. Wang, Q. Yan, C. Yu, J. Chen, G. Xu, L. He, L. Li, L. Chen, A. Giles Davies, E. H. Linfield, J. Hao, P.-B. Vigneron, and R. Colombelli, Appl. Phys. Lett. **109**, 231105 (2016).
5. N. Jukam, S. S. Dhillon, D. Oustinov, J. Madeo, C. Manquest, S. Barbieri, C. Sirtori, S. P. Khanna, E. H. Linfield, A. G. Davies, and J. Tignon, Nat. Photonics **3**, 715 (2009).
6. S. S. Dhillon, S. Sawallich, N. Jukam, D. Oustinov, J. Madéo, S. Barbieri, P. Filloux, C. Sirtori, X. Marcadet, and J. Tignon, Appl. Phys. Lett. **96**, 061107 (2010).
7. H. Ghafouri-Shiraz, *Fundamentals of Laser Diode Amplifiers* (Wiley, 1996), Chap. 3.
8. R. Rungsawang, N. Jukam, J. Maysonnave, P. Cavalié, J. Madéo, D. Oustinov, S. S. Dhillon, J. Tignon, P. Gellie, C. Sirtori, S. Barbieri, H. E. Beere, and D. A. Ritchie, Appl. Phys. Lett. **98**, 101102 (2011).
9. F. Raineri, G. Vecchi, C. Cojocaru, A. M. Yacomotti, C. Seassal, X. Letartre, P. Viktorovitch, R. Raj, and A. Levenson, Appl. Phys. Lett. **86**, 091111 (2005).
10. S. Kumar, B. S. Williams, Q. Qin, A. W. M. Lee, Q. Hu, and J. L. Reno, Opt. Express **15**, 113 (2007).
11. T.-Y. Kao, X. Cai, A. W. M. Lee, J. L. Reno, and Q. Hu, Opt. Express **23**, 17091 (2015).
12. D. Rutledge, *Grid Amplifiers*, NATO ASI Series (Springer Netherlands, 1997), Vol. **334**, p. 221.
13. J. Madéoa, Y. Todorov, and C. Sirtori, Appl. Phys. Lett. **104**, 031108 (2014).
14. D. Palaferri, Y. Todorov, A. Mottaghizadeh, G. Frucci, G. Biasiol, and C. Sirtori, New J. Phys. **18**, 113016 (2016).
15. D. Burghoff, T.-Y. Kao, D. Ban, A. W. M. Lee, Q. Hu, and J. Reno, Appl. Phys. Lett. **98**, 061112 (2011).
16. H. Callebaut and Q. Hu, J. Appl. Phys. **98**, 104505 (2005).
17. T.-Y. Kao, J. L. Reno, and Q. Hu, Nat. Photonics **10**, 541 (2016).
18. H.-T. Chen, J. F. O'Hara, A. K. Azad, A. J. Taylor, R. D. Averitt, D. B. Shrekenhamer, and W. J. Padilla, Nat. Photonics **2**, 295 (2008).
19. H.-T. Chen, A. J. Taylor, and N. Yu, Rep. Prog. Phys. **79**, 7 (2016).
20. L. Xu, C. A. Curwen, P. W. C. Hon, Q.-S. Chen, T. Itoh, and B. S. Williams, Appl. Phys. Lett. **107**, 221105 (2015).